Compressible turbulent mixing: Effects of compressibility

Qionglin Ni*

Department of Physics, University of Rome Tor Vergata, Via della Ricerca Scientifica 1, 00133, Rome, Italy;
State Key Laboratory for Turbulence and Complex Systems, College of Engineering, Peking University, 100871, Beijing, People's Republic of China;
and Department of High Performance Server Business, Inspur Group, 100085, Beijing, People's Republic of China

(Received 23 July 2015; revised manuscript received 1 April 2016; published 18 April 2016)

We studied by numerical simulations the effects of compressibility on passive scalar transport in stationary compressible turbulence. The turbulent Mach number varied from zero to unity. The difference in driven forcing was the magnitude ratio of compressive to solenoidal modes. In the inertial range, the scalar spectrum followed the $k^{-5/3}$ scaling and suffered negligible influence from the compressibility. The growth of the Mach number showed (1) a first reduction and second enhancement in the transfer of scalar flux; (2) an increase in the skewness and flatness of the scalar derivative and a decrease in the mixed skewness and flatness of the velocity-scalar derivatives; (3) a first stronger and second weaker intermittency of scalar relative to that of velocity; and (4) an increase in the intermittency parameter which measures the intermittency of scalar in the dissipative range. Furthermore, the growth of the compressive mode of forcing indicated (1) a decrease in the intermittency parameter and (2) less efficiency in enhancing scalar mixing. The visualization of scalar dissipation showed that, in the solenoidal-forced flow, the field was filled with the small-scale, highly convoluted structures, while in the compressive-forced flow, the field was exhibited as the regions dominated by the large-scale motions of rarefaction and compression.

DOI: 10.1103/PhysRevE.93.043116

I. INTRODUCTION

Turbulent mixing is the process that includes the generation of scalar fluctuations, distortion of scalar interfaces, and creation of scalar gradients at small scales. For incompressible flows, the classical picture of scalar transport is that the scalar fluctuations are generated at large scales and transported through successive breakdowns into smaller scales; the process proceeds until the scalar fluctuations are homogenized and dissipated by molecular diffusion at the smallest scale. Compressible turbulent motion is of fundamental importance in many natural phenomena and industrial applications. Therefore, an understanding of passive scalar physics in compressible flows is crucial in many fields, including the scattering of interstellar materials in galaxies, dispersion of air pollutants in the atmosphere, and combustion of chemical reactions in an aircraft engine [1–6]. Hereafter, we omit the term "passive" where there is no ambiguity. Previous simulations [7] computed the time scale of the scalar variance decaying in an interstellar turbulence, but did not provide a detailed discussion of turbulent mixing. Other simulations based on the piecewise-parabolic method [8,9] showed that, for velocity, the compressive component is less efficient than the solenoidal component in enhancing mixing. The cascade of scalar is similar to that of velocity, as long as the time scales of scalar and velocity dissipations are comparable. Moreover, the scaling of scalar structure function corresponds well to the SL94 model [10]. Our recent studies on scalar mixing in compressible turbulence [11–13] found that (1) the scalar spectrum follows a $k^{-5/3}$ power law in the inertial-convective range. At high and low Schmidt numbers, it also defers to a k^{-1} power law in the viscous-convective range and a $k^{-17/3}$ power law in the inertial-diffusive range, respectively, where k is the wave number; (2) for the scalar transport, the advection and dissipation terms follow the Kolmogorov picture; (3) the cascade of passive scalar is mainly determined by the solenoidal component of velocity, while that of active scalar is dominated by the compressive component of velocity; and (4) when the degree of compressibility is sufficiently strong, an inverse cascade develops for the passive scalar at large scales.

On the other hand, previous studies of compressible turbulence demonstrated that the degree of compressibility is controlled by two factors [8,9,14]: one is the Mach number and the other is the forcing scheme. In detail, the degree of compressibility is enhanced by the growth of the Mach number. For the same Mach number, a flow driven by a compressive mode of forcing usually provides more compressibility than that driven by a solenoidal mode of forcing. Nevertheless, the same variation of compressibility caused by the above two factors may have different effects on the scalar statistics. In this paper, we performed numerical studies for compressible turbulent mixing, using a novel computational approach [15]. To examine the effects of compressibility on the scalar transport in turbulence, both incompressible and compressible flows were solved, and the range of the turbulent Mach number (M_t) was $0.23 \sim 1.02$. These flows were driven by the large-scale solenoidal mode of forcing [12,16]. Simultaneously, we also performed two compressible flows driven by both the large-scale solenoidal and compressive modes of forcing [11,14], where the values of M_t were fixed at 0.6. This paper is part of a systematic investigation of the effects of basic parameters on compressible turbulent mixing. In a companion paper [11], we have carefully examined the Schmidt number effects.

The rest of this paper is organized as follows: the governing equations and simulated parameters are described in Sec. II. In Sec. III we analyze the effects of compressibility from the change in the Mach number, and that caused by the difference

*niql.pku@gmail.com

in the forcing scheme is reported in Sec. IV. The summary and conclusions regarding this paper are given in Sec. V.

II. GOVERNING EQUATIONS AND SIMULATED PARAMETERS

We consider a statistically stationary system of passive scalar transport in the compressible turbulence of an ideal gas. The velocity and scalar fields are driven and maintained by large-scale, random forcing. The accumulated internal energy at small scales is removed by a cooling function added at large scales. Based on the basic scales of L for length, ρ_0 for density, U for velocity, T_0 for temperature, and ϕ for scalar, the governing equations and the state equation of ideal gas, in dimensionless form, are written as

$$\frac{\partial \rho}{\partial t} + \frac{\partial(\rho u_j)}{\partial x_j} = 0, \tag{2.1}$$

$$\frac{\partial(\rho u_i)}{\partial t} + \frac{\partial[\rho u_i u_j + p\delta_{ij}/\gamma M^2]}{\partial x_j} = \frac{1}{\mathrm{Re}}\frac{\partial \sigma_{ij}}{\partial x_j} + \rho \mathcal{F}_i, \tag{2.2}$$

$$\frac{\partial \mathcal{E}}{\partial t} + \frac{\partial[(\mathcal{E} + p/\gamma M^2)u_j]}{\partial x_j} = \frac{1}{\alpha}\frac{\partial}{\partial x_j}\left(\kappa \frac{\partial T}{\partial x_j}\right) + \frac{1}{\mathrm{Re}}\frac{\partial(\sigma_{ij}u_i)}{\partial x_j} - \Lambda + \rho \mathcal{F}_j u_j, \tag{2.3}$$

$$\frac{\partial(\rho\phi)}{\partial t} + \frac{\partial[(\rho\phi)u_j]}{\partial x_j} = \frac{1}{\beta}\frac{\partial}{\partial x_j}\left(\rho\chi \frac{\partial \phi}{\partial x_j}\right) + \rho \mathcal{S}, \tag{2.4}$$

$$p = \rho T. \tag{2.5}$$

The primary variables are the density ρ, velocity vector $\mathbf{u}$, pressure p, temperature T, and scalar ϕ. The nondimensional parameters α and β are $\alpha = \mathrm{Pr}\,\mathrm{Re}(\gamma-1)M^2$ and $\beta = \mathrm{Sc}\,\mathrm{Re}(\gamma-1)\gamma$. $\mathcal{F}_j$ is the dimensionless large-scale velocity forcing:

$$\mathcal{F}_j = \sum_{l=1}^{2} \hat{\mathcal{F}}_j(\mathbf{k}_l)\exp(i\mathbf{k}_l\mathbf{x}) + \mathrm{c.c.}, \tag{2.6}$$

where $\hat{\mathcal{F}}_j$ is the Fourier amplitude, which may have the solenoidal and compressive modes perpendicular and parallel to $\mathbf{k}_l$, respectively. $\mathbf{k}_l$ is the wave number vector in Cartesian coordinate, and a growth of the index l indicates an increase in wave number. Similarly, the dimensionless large-scale scalar forcing $\mathcal{S}$ is written as

$$\mathcal{S} = \sum_{l=1}^{2} \hat{\mathcal{S}}(\mathbf{k}_l)\exp(i\mathbf{k}_l\mathbf{x}) + \mathrm{c.c.}, \tag{2.7}$$

where the Fourier amplitude $\hat{\mathcal{S}}$ is perpendicular to $\mathbf{k}_l$. A detailed discussion of the cooling function Λ can be found in Ref. [15]. The expressions for the viscous stress σ_{ij} and the total energy per unit volume $\mathcal{E}$ are

$$\sigma_{ij} = \mu\left(\frac{\partial u_i}{\partial x_j} + \frac{\partial u_j}{\partial x_i}\right) - \frac{2}{3}\mu\theta\delta_{ij}, \tag{2.8}$$

$$\mathcal{E} = \frac{p}{(\gamma-1)\gamma M^2} + \frac{1}{2}\rho(u_j u_j). \tag{2.9}$$

Here $\theta = \partial u_k/\partial x_k$ is the velocity divergence or dilatation. $M \equiv U/c_0$ is the reference Mach number, $c_0 \equiv \sqrt{\gamma R T_0}$ is the reference sound speed, and $\gamma \equiv C_p/C_v$ is the ratio of specific heat at constant pressure to that at constant volume. We shall assume that both specific heats are independent of temperature, which is a reasonable assumption for the air temperature in the simulations within the current Mach number range [15]. Three additional basic parameters are the reference Reynolds number $\mathrm{Re} \equiv \rho_0 U L/\mu_0$, the reference Prandtl number $\mathrm{Pr} \equiv \mu_0 C_p/\kappa_0$, and the reference Schmidt number $\mathrm{Sc} \equiv \nu_0/\chi_0$, where $\nu_0 \equiv \mu_0/\rho_0$ is the reference kinematic viscosity. In this study, the values of γ, Pr, and Sc are set as 1.4, 0.7, and 1.0, respectively. Thus, there remain two independent parameters of M and Re to control the system. For completion, we employ the Sutherland law [17] to specify the temperature-dependent dynamical viscosity, thermal conductivity, and molecular diffusivity as

$$\mu, \kappa, \chi = \frac{1.4042 T^{1.5}}{T + 0.4042}. \tag{2.10}$$

The system is solved numerically in a cubic box with periodic boundary conditions, by adopting a new computational method. This method utilizes a seventh-order weighted essentially nonoscillatory (WENO) scheme [18] for shock regions, and an eighth-order compact central finite difference (CCFD) scheme [19] for smooth regions outside shocks. A flux-based conservative formulation is employed to optimize the interface between the two regions and thus improve the computational efficiency. The details of the computational method can be found in Ref. [15]. Furthermore, in simulation computations it is usual to use the turbulent Mach number $M_t \equiv Mu'/\langle\sqrt{T}\rangle$ and the Taylor microscale Reynolds number $\mathrm{Re}_\lambda \equiv \mathrm{Re}\,u'\lambda\langle\rho\rangle/\sqrt{3}\langle\mu\rangle$ rather than the reference Mach number and the reference Reynolds number to describe the flow, where u' is the root-mean-square (r.m.s.) velocity magnitude (defined below) and $\lambda \equiv u'/\sqrt{\langle(\partial u_j/\partial x_j)^2\rangle}$ is the Taylor microscale.

Table I presents the major simulated parameters. The simulations are conducted on a $N^3 = 512^3$ grid and are divided into two groups according to the source of compressibility. The first group, including R1S, R2S, R3S, and R4S, is used to study the variation of compressibility caused by the change in the Mach number, where M_t increases from zero to unity. Note that the incompressible flow (R1S) is also solved numerically in a cubic box with periodic boundary conditions but by adopting a different computational method of pseudo spectral scheme. In the second group, R3S, R3Ca, and R3Cb, M_t is fixed at around 0.6; we study the variation of compressibility because of the difference in the forcing scheme. In R3S the Fourier amplitude of the forcing function has only the solenoidal mode, while in R3Ca and R3Cb, it additionally has the compressive mode. The ratios of solenoidal to compressive modes are 1.00 in R3Ca and 0.05 in R3Cb, respectively. Moreover, in the above six simulation cases, the values of Re_λ are around 180, and those of the Kolmogorov scale $\eta \equiv [\langle\mu/(\mathrm{Re}\rho)\rangle^3/\langle\epsilon/\rho\rangle]^{1/4}$ are 0.01, where $\epsilon \equiv \sigma_{ij}S_{ij}/\mathrm{Re}$ is the kinetic energy dissipation rate. In addition, we introduce the quantity ϖ to measure compressibility, which is defined as [20]

$$\varpi \equiv \frac{\left\langle\left(\frac{\partial u_i}{\partial x_i}\right)^2\right\rangle}{\left\langle\left(\frac{\partial u_i}{\partial x_j}\right)^2\right\rangle}. \tag{2.11}$$

TABLE I. Flow statistics in the simulations.

Case	M_t	Re_λ	η	u'	ϕ'	ρ'	E_K	E_ϕ	$\langle\epsilon\rangle$	$\langle\epsilon_\phi\rangle$	ϖ
R1S	0	179	0.01	2.30	2.34	0	2.66	2.74	0.78	1.62	0
R2S	0.23	181	0.01	2.28	2.29	0.02	2.58	2.63	0.73	1.70	0.003
R3S	0.62	183	0.01	2.32	2.28	0.12	2.62	2.60	0.75	1.63	0.02
R4S	1.02	178	0.01	2.21	2.25	0.29	2.31	2.48	0.56	1.45	0.11
R5S	0.02	186	0.01	2.29	2.32	0.0005	2.59	2.69	0.76	1.75	0.0002
R3Ca	0.60	179	0.01	2.22	2.28	0.30	2.39	2.62	0.69	1.42	0.18
R3Cb	0.61	180	0.01	2.17	2.23	0.44	2.36	2.55	0.71	1.18	0.35

For the first group, ϖ increases as M_t increases. In the low M_t flow, i.e., R2S, the value of ϖ is very small. In contrast, for the second group, M_t significantly increases when the compressive mode of the forcing increases. This indicates that ϖ is better than M_t to parametrize the compressibility of compressible turbulence.

The remainder of the simulated parameters in Table I show that the r.m.s. magnitude of scalar ($\phi' \equiv \sqrt{\langle\phi^2\rangle}$) and the scalar variance per unit volume ($E_\phi \equiv \langle\rho\phi^2\rangle/2$) decrease when M_t increases from zero to unity. In contrast, the r.m.s. magnitude of velocity ($u' \equiv \sqrt{\langle u_j^2\rangle}$) and the kinetic energy per unit volume ($E_K \equiv \langle\rho u_j^2\rangle/2$) decrease when the compressive mode of the forcing increases. The r.m.s. magnitude of density fluctuations [$\rho' \equiv \sqrt{\langle(\rho - \langle\rho\rangle)^2\rangle}$] increases when M_t increases from zero to unity and increases significantly when the compressive mode of forcing increases. This indicates that the intensity of density fluctuations sensitively increases as the degree of compressibility grows. Here the sign $\langle\cdot\rangle$ denotes ensemble average, and the repetition on subscript denotes the Einstein summation. The ensemble average of the scalar dissipation rate [$\epsilon_\phi \equiv \chi(\partial\phi/\partial x_j)^2$] is found to decrease as the compressive mode of the forcing increases. This implies that the compressive mode is less efficient than the solenoidal mode in enhancing scalar dissipation.

III. EFFECTS OF COMPRESSIBILITY: CHANGE IN THE MACH NUMBER

A. Fundamental statistics

In this section we focus on the effects of compressibility on compressible turbulent mixing caused by the change in the Mach number. The Kolmogorov theory is a milestone in turbulence research [21,22]. It predicts that, in the inertial range of $L_f^{-1} \ll k \ll \eta^{-1}$, the energy spectrum of incompressible turbulence is

$$E(k) = C_K \langle\epsilon\rangle^{2/3} k^{-5/3}, \tag{3.1}$$

where L_f is the integral length scale of velocity, C_K is the Kolmogorov constant, and the typical values are 1.5–2.0 [23]. For compressible turbulence, an operational definition of the inertial range can be constructed in a similar way, and the compensated energy spectra according to the Kolmogorov variables at different M_t are shown in Fig. 1. Obviously, for the energy spectra, plateaus appear in the inertial range of $5 \leqslant k \leqslant 20$, and the values of C_K are about 2.07. Throughout the entire wave number range, the energy spectra from the four simulation cases overlap, except that at high wave numbers the energy content in R4S decays a bit faster. It reveals that, in our simulations, the change in the Mach number brings little contribution to the energy spectrum.

By applying the Kolmogorov theory to the scalar transport in an incompressible flow, Obukhov [24] and Corrsin [25] derived a scalar spectrum in the inertial range satisfying $L_\phi^{-1} \ll k \ll \eta^{-1}$:

$$E_\phi(k) = C_\phi \langle\epsilon_\phi\rangle \langle\epsilon\rangle^{-1/3} k^{-5/3}, \tag{3.2}$$

where L_ϕ is the integral length scale of scalar, C_ϕ is the Obukhov-Corrsin (OC) constant, and the typical values are 0.75–0.92 in experiments [26] and 0.87 ± 0.10 in simulations [27], respectively. Figure 2 shows the compensated scalar spectra according to the OC variables at different M_t. For the scalar spectra of compressible flows, the plateaus appear in the same inertial range of $5 \leqslant k \leqslant 20$, and the values of C_{OC} are about 0.83. In contrast, for the scalar spectrum of incompressible flow, the inertial-range plateau is found in the higher wave number range of $12 \leqslant k \leqslant 30$, and C_{OC} is about 1.15, significantly larger. In addition, the scalar spectra of compressible flows almost overlap, except that at high wave numbers the energy content in R4S decays a bit faster. In contrast, in the incompressible flow, the spectral bump at high wave numbers is quite conspicuous, causing the energy content to decay more slowly in the dissipative range.

In order to prove that, in this study, the transition from incompressible to compressible turbulence is smooth, we provide a supplementary simulation case, R5S, where

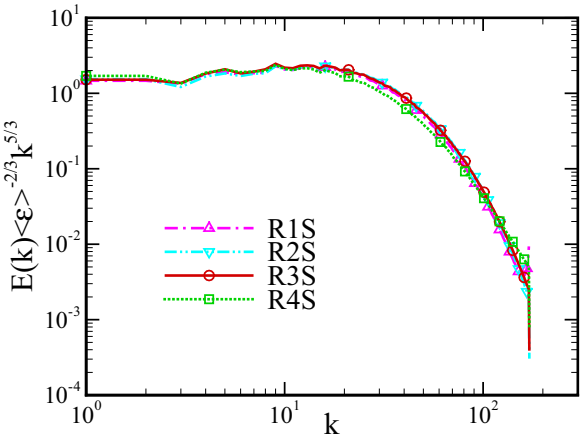

FIG. 1. Compensated spectrum of kinetic energy according to the Kolmogorov variables.

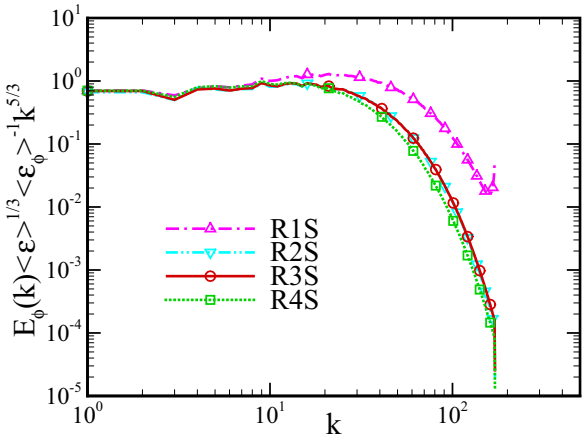

FIG. 2. Compensated spectrum of scalar according to the Obukhov-Corrsin variables.

$M_t = 0.02$ and $\mathrm{Re}_\lambda = 186$. In Figs. 3(a) and 3(b) we plot the compensated energy and scalar spectra from R1S, R2S, and R5S, respectively. In the entire wave number range, the energy spectra from the three simulation cases almost overlap, indicating that the transition from incompressible to compressible flows is smooth. In contrast, we observe several differences in the scalar spectra from the three simulation cases. For R1S and R5S, the spectra are close to each other in the inertial range and separate from each other in the dissipative range. For R2S and R5S, the spectra almost overlap in the dissipative range, exhibiting universal features in that range. Compared with energy spectrum, in weakly compressible turbulence, the relatively stronger response of scalar to the compressibility is attributed to the stronger intermittency of scalar.

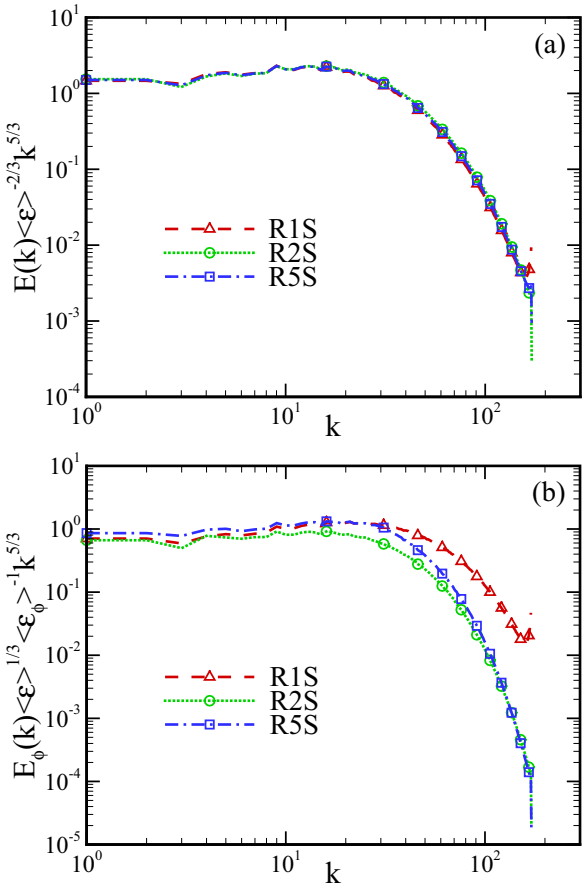

FIG. 3. (a) Compensated spectrum of kinetic energy according to the Kolmogorov variables, from cases of R1S, R2S, and R5S. (b) Compensated spectrum of scalar according to the Obukhov-Corrsin variables, from cases of R1S, R2S, and R5S.

Instead of the three-dimensional (3D) scalar spectrum, in experiments one always measures the one-dimensional (1D) counterpart, which for isotropic turbulence is written as

$$E_{1\phi}(k) = -\int_k^\infty \frac{E_\phi(k)}{k}\, dk. \tag{3.3}$$

In Fig. 4 we plot the 1D compensated scalar spectra at different M_t. We have taken averages over three coordinate directions. The spectral bump, which is a precursor to the k^{-1} part of the scalar spectrum, has been found in previous studies of incompressible turbulent mixing. Here we also observe it in the 1D scalar spectrum from compressible turbulent mixing. Furthermore, the 1D OC constant ($C_{1\phi}$) can be obtained using Eq. (3.3), and it is connected with the 3D OC constant at $C_{1\phi} = 3C_\phi/5$. Figure 4 shows that this relation is satisfied in our simulations.

The equivalence of the scalar spectrum in physical space is the second-order structure function of scalar increment, which is defined as

$$S_{\phi 2}(r) \equiv \langle (\delta_r \phi)^2 \rangle, \tag{3.4}$$

where $\delta_r \phi = \phi(\mathbf{x} + r) - \phi(\mathbf{x})$ is the scalar increment. In Fig. 5 we plot $S_{\phi 2}(r)$ normalized by the OC variables, as suggested in Eq. (3.2), as function of the normalized separation distance r/η. The figure shows that, in the inertial range of $30 \leqslant r/\eta \leqslant 150$, plateaus appear with finite widths. The values of the scaling constant computed from plateaus are defined as

$$C_s = \frac{S_{\phi 2}(r)}{r^{2/3}\langle \epsilon \rangle^{-1/3} \langle \epsilon_\phi \rangle} \tag{3.5}$$

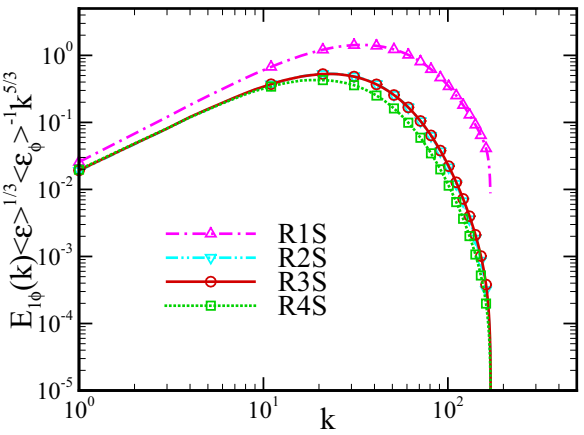

FIG. 4. One-dimensional compensated spectrum of scalar according to the Obukhov-Corrsin variables.

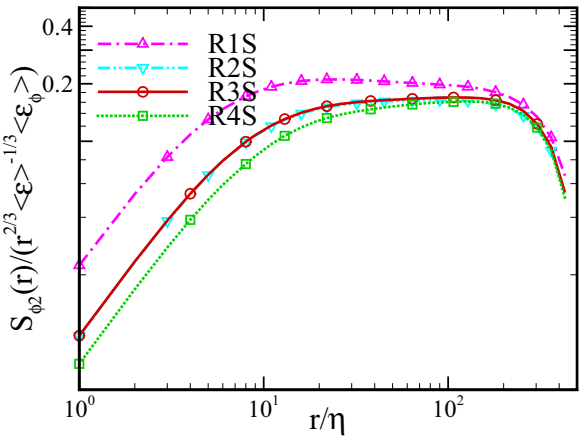

FIG. 5. Obukhov-Corrsin scaling of second-order structure function of scalar.

and are 0.20, 0.16, 0.17, and 0.15 from R1S through R4S, respectively. It reveals that the second-order structure function of scalar increment is insensitive to the current change in the Mach number, except for the transition from incompressible to compressible flows.

The mixed third-order structure function is defined as

$$S_{m3}(r) \equiv \langle \delta_r u (\delta_r \phi)^2 \rangle, \tag{3.6}$$

where $\delta_r u = u(\mathbf{x}+r) - u(\mathbf{x})$ is the longitudinal velocity increment, and plays a more fundamental role in the similarity scaling. In incompressible turbulence, Yaglom [28] derived the following exact result for the range of $\mathrm{Sc}^{-1/2}\eta \ll r \ll L_\phi$:

$$\langle \delta_r u (\delta_r \phi)^2 \rangle = -\tfrac{4}{3} \langle \epsilon_\phi \rangle r. \tag{3.7}$$

In this study, the value of the Schmidt number (Sc) is set as unity. Figure 6 presents the minus of $S_{m3}(r)$ normalized by the Yaglom variables. It is found that, for each simulated flow, a flat region appears with finite width. At large scales, $-S_{m3}(r)$ drops and approaches zero, while at small scales, it behaves approximately as r^2 according to the Taylor expansion. We

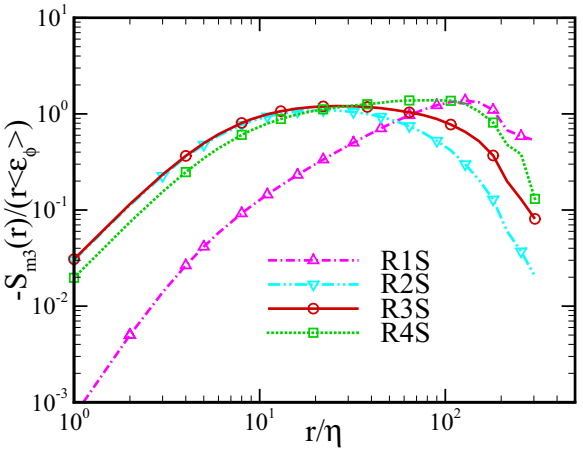

FIG. 6. Yaglom scaling of mixed third-order velocity-scalar structure function.

compute the scaling constant of $S_{m3}(r)$ as

$$C_m = -\frac{S_{m3}}{r\langle \epsilon_\phi \rangle}. \tag{3.8}$$

Our results show that, in flat regions, the values of C_m are 1.31, 1.10, 1.19, and 1.37 from R1S through R4S, respectively. Since the mixed third-order velocity-scalar structure function corresponds to the scalar flux in physical space, it is concluded in two aspects: (1) the transition from incompressible to compressible flows leads the transfer of scalar flux to being reduced and (2) for compressible flow, the transfer of scalar flux is enhanced as the Mach number increases.

At the end of this subsection, the two-dimensional (2D) isocontour lines of scalar fields in the $z = \pi/2$ plane from R1S and R4S are depicted in Fig. 7. Obviously, the scalar field from the incompressible flow is full of the small-scale "ramp-cliff" structures. For the $M_t = 1.02$ compressible flow, although

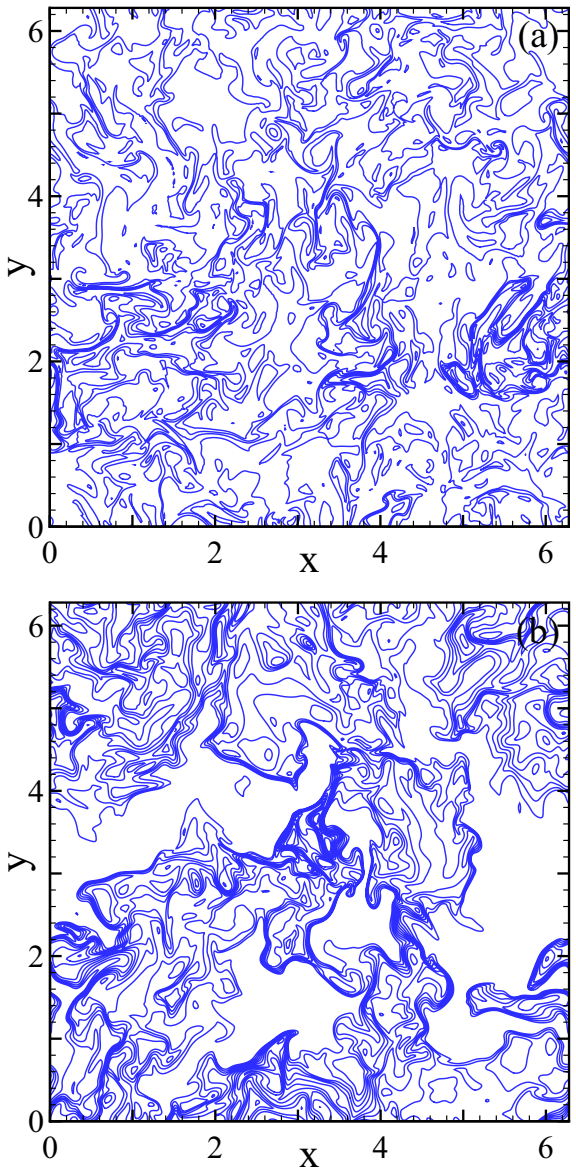

FIG. 7. Two-dimensional isocontour lines of scalar field from (a) R1S and (b) R4S, in $z = \pi/2$.

there are small-scale "ramp-cliff" structures, the scalar field is globally divided into the large-scale regions of rarefaction and compression.

B. Higher-order statistics

For higher-order statistics, the skewness and flatness of scalar increment, displaying the change of the distribution of scalar field, are defined as

$$K_3(r) \equiv \frac{\langle(\delta_r\phi)^3\rangle}{\langle(\delta_r\phi)^2\rangle^{3/2}}, \tag{3.9}$$

$$K_4(r) \equiv \frac{\langle(\delta_r\phi)^4\rangle}{\langle(\delta_r\phi)^2\rangle^2}. \tag{3.10}$$

In Fig. 8 we plot the skewness (top) and flatness (bottom) of $\delta_r\phi$ against the normalized separation distance r/η. At small scales, the skewness from incompressible flow is positive, while that from compressible flows is negative. When scale increases, the magnitude of skewness falls and approaches zero. At large scales, the skewness oscillates around zero. In addition, throughout scale ranges, the magnitude of skewness from the high M_t flow is always larger than that from the low M_t flow. However, the magnitude of skewness from the middle M_t flow is first larger and then smaller than that from the low M_t flow. In terms of flatness, it is close to each other

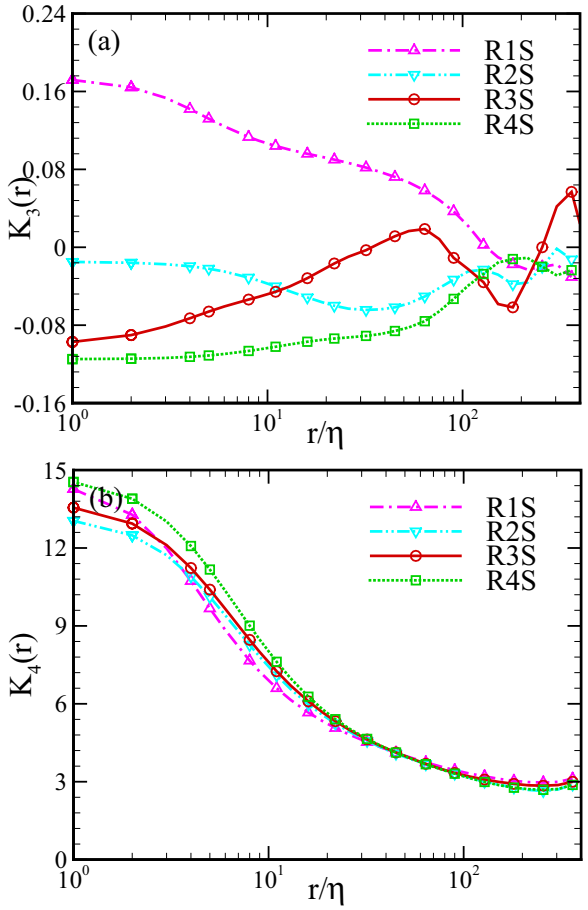

FIG. 8. (a) Skewness of scalar increment as a function of r/η. (b) Flatness of scalar increment as a function of r/η.

TABLE II. Skewness and flatness in the simulations.

Case	S_u	S_ϕ	$S_{u\phi}$	F_u	F_ϕ	$F_{u\phi}$
R1S	−0.13	0.17	−0.49	14.7	15.6	1.9
R2S	−0.51	−0.03	−0.49	5.8	13.7	1.9
R3S	−0.52	−0.09	−0.45	5.9	14.2	1.9
R4S	−1.72	−0.11	−0.36	21.8	14.9	1.8
R3Ca	−4.70	−0.13	−0.39	97.3	16.4	1.8
R3Cb	−11.66	−0.19	−0.31	274.1	18.2	1.7

at small scales, and decreases and approaches 3.0 as scale increases. Note that the 3.0 value stands for the Gaussian distribution without intermittency.

We now compute the skewness and flatness of scalar derivative as

$$S_\phi \equiv \frac{\left[\langle\sum_j\left(\frac{\partial\phi}{\partial x_j}\right)^3\rangle\right]/3}{\left[\langle\sum_j\left(\frac{\partial\phi}{\partial x_j}\right)^2\rangle/3\right]^{3/2}}, \quad F_\phi \equiv \frac{\left[\langle\sum_j\left(\frac{\partial\phi}{\partial x_j}\right)^4\rangle\right]/3}{\left[\langle\sum_j\left(\frac{\partial\phi}{\partial x_j}\right)^2\rangle/3\right]^2}. \tag{3.11}$$

Also, the mixed skewness and flatness of velocity-scalar derivatives are defined as

$$S_{u\phi} \equiv \frac{\left[\langle\sum_j\frac{\partial u_j}{\partial x_j}\left(\frac{\partial\phi}{\partial x_j}\right)^2\rangle\right]/3}{\left[\langle\sum_j\left(\frac{\partial u_j}{\partial x_j}\right)^2\rangle/3\right]^{1/2}\left[\langle\sum_j\left(\frac{\partial\phi}{\partial x_j}\right)^2\rangle/3\right]}, \tag{3.12}$$

$$F_{u\phi} \equiv \frac{\left[\langle\sum_j\left(\frac{\partial u_j}{\partial x_j}\right)^2\left(\frac{\partial\phi}{\partial x_j}\right)^2\rangle\right]/3}{\left[\langle\sum_j\left(\frac{\partial u_j}{\partial x_j}\right)^2\rangle/3\right]\left[\langle\sum_j\left(\frac{\partial\phi}{\partial x_j}\right)^2\rangle/3\right]}, \tag{3.13}$$

where $j = 1$, 2, and 3. Table II lists the values of S_ϕ, $S_{u\phi}$, F_ϕ, and $F_{u\phi}$. Here we also present the values of S_u and F_u. Their definitions are similar to those of S_ϕ and F_ϕ. These values show that the skewness of scalar derivative changes from positive to negative when the flow transits from incompressible to compressible. More importantly, when the degree of compressibility grows, the magnitudes of the skewness and flatness of scalar derivative increase, but those of the mixed skewness and flatness of velocity-scalar derivatives decrease. For each compressible flow, the magnitude of the skewness of velocity derivative is always larger than that of the skewness of scalar derivative. The comparison between F_ϕ and F_u shows that, for the flow with a low degree of compressibility, the intermittency of scalar is stronger than that of velocity. This relation reverses if the degree of compressibility continuously grows.

The structure functions for the scalar increment and the mixed velocity-scalar increments are defined as

$$S_p(r) \equiv \langle|\delta_r\phi|^p\rangle, \tag{3.14}$$

$$S_{mp}(r) \equiv \langle|\delta_r u(\delta_r\phi)^2|^{p/3}\rangle, \tag{3.15}$$

where p is the order number. For simplicity, in Eq. (3.15) we have assumed isotropy and dropped any possible dependency on the velocity component. Given the values of the Reynolds number in our simulations, it is better to study the relative scaling properties using a procedure known as extended self-similarity (ESS) [29]. In Fig. 9 we plot the ESS type $S_p(r)$ (top) and $S_{mp}(r)$ (bottom) against the normalized separation distance

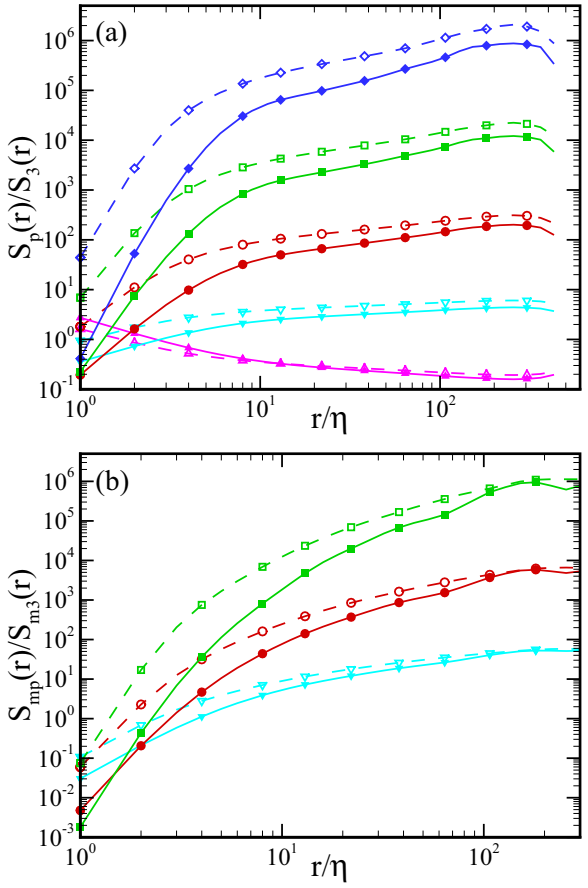

FIG. 9. (a) ESS structure functions of scalar from R1S (dashed lines) and R4S (solid lines), where the symbols of deltas, gradients, circles, squares, and diamonds are for $p = 2$, 4, 6, 8, and 10, respectively. (b) ESS mixed structure functions of velocity scalar from R1S (dashed lines) and R4S (solid lines), where the symbols of gradients, circles, and squares are for $p = 6$, 9, and 12, respectively.

r/η, at $p = 2$, 4, 6, 8, 10, and $p = 6$, 9, 12, respectively. When p grows, the difference of $S_p(r)/S_3(r)$ between the incompressible flow and the $M_t = 1.02$ compressible flow increases. At every p, the inertial-range slope of $S_p(r)/S_3(r)$ from the incompressible flow is smaller than that from the $M_t = 1.02$ compressible flow. For $S_{mp}(r)/S_{m3}(r)$, it displays behavior similar to $S_p(r)/S_3(r)$.

The scaling exponents of $S_p(r)$, which are computed by taking averages of the local scaling exponents

$$\zeta_p(r) \equiv \frac{d\log[S_p(r)]}{d\log(r/\eta)}, \tag{3.16}$$

are depicted in Fig. 10, as a function of the order number p. For comparison, we present the scaling exponents from the isothermal compressible flows [9] and incompressible flow [30]. It shows that at large order numbers: (1) for incompressible flow, $\zeta(p)$ from R1S is significantly smaller than that from Ref. [30], while for compressible flow, $\zeta(p)$ from R4S, where $M_t = 1.02$, is a bit larger than that from the $M_t = 0.9$ isothermal case; and (2) $\zeta(p)$ from Ref. [30] and the $M_t = 6.1$ isothermal case have the largest and smallest values, respectively, while $\zeta(p)$ from R1S collapses between

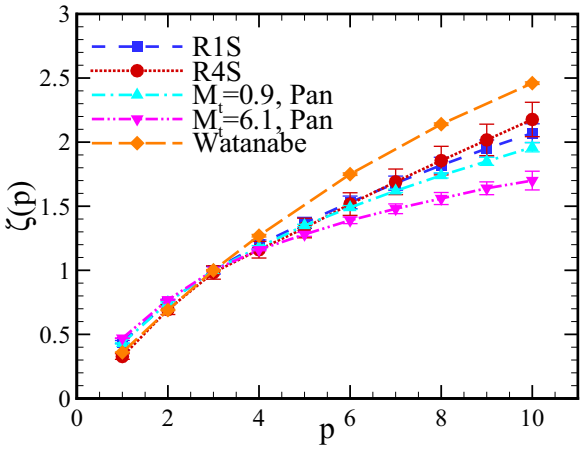

FIG. 10. Scaling exponents of structure function of scalar against the order number p.

those from R4S and the $M_t = 0.9$ isothermal case. Figure 11 shows the scaling exponents of $S_{mp}(r)$, which are computed by taking averages of the local scaling exponents

$$\zeta_{mp}(r) \equiv \frac{d\log[S_{mp}(r)]}{d\log(r/\eta)}. \tag{3.17}$$

At large order numbers, $\zeta_m(p)$ from R4S and the $M_t = 6.1$ isothermal case have the largest and smallest values, respectively, and $\zeta_m(p)$ from R1S collapses between those from R4S and the $M_t = 0.9$ isothermal case. The above results show that, in this study, for the inertial range, the intermittency of scalar in the incompressible flow is stronger than that in the $M_t = 1.02$ compressible flow, which is also confirmed by the values of the flatness of scalar derivative listed in Table II.

C. Dissipation and mixing time scale

In a turbulent flow, the scalar dissipation fluctuates in space. These fluctuations are regarded as the exhibition of the intermittency of scalar. Thus, it is valuable to study the spatial structure of scalar dissipation. In Fig. 12 we depict the 2D contours of the logarithms of the scalar dissipation rate in

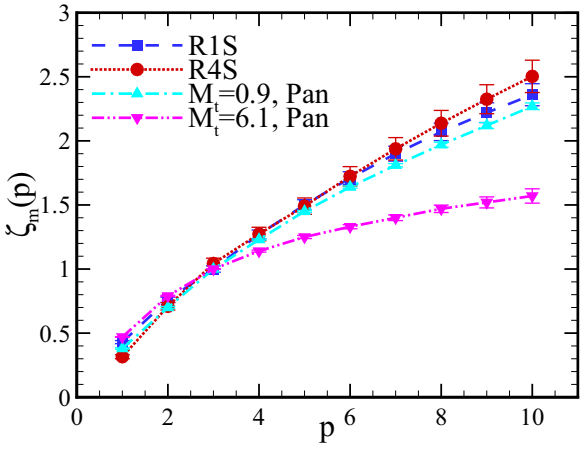

FIG. 11. Scaling exponents of mixed structure function of velocity scalar against the order number p.

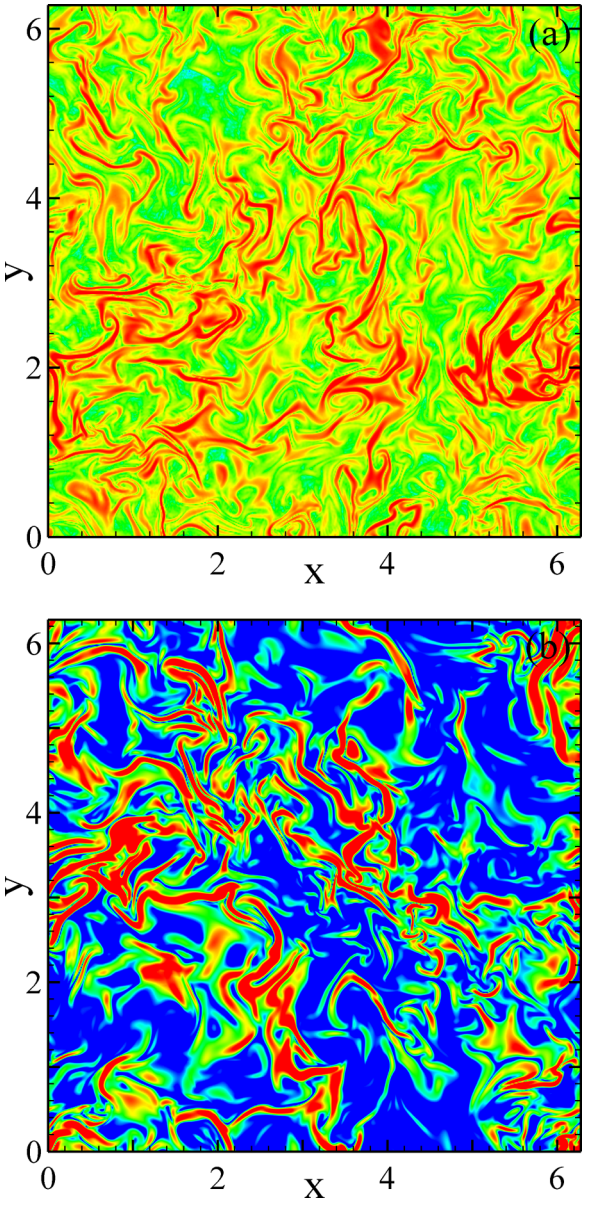

FIG. 12. Two-dimensional contours of logarithm of scalar dissipation rate from (a) R1S and (b) R4S, in $z = \pi/2$, where the logarithmic base is 10.

the $z = \pi/2$ plane from R1S and R4S, where the color scale is determined as

$$\psi = \log_{10}(D/D'). \tag{3.18}$$

Here $D = \chi(\partial\phi/\partial x_j)^2/\beta$, and $D' = \sqrt{\langle (D - \langle D\rangle)^2\rangle}$ is the r.m.s. magnitude of D. The color changes from blue to red as dissipation increases. In the incompressible flow, the scalar dissipation field is full of the small-scale, high-dissipation structures, which are very sharp and highly convoluted, and are displayed as random distribution. In the $M_t = 1.02$ compressible flow, although the high-dissipation structures are highly convoluted, they are larger in scale and width and are displayed as rare random distribution. This indicates that the shocklet structures enhance the scalar dissipation in the convoluted regions. Moreover, the magnitude of the smooth, low-dissipation regions from the $M_t = 1.02$ compressible flow is smaller than that from the incompressible flow.

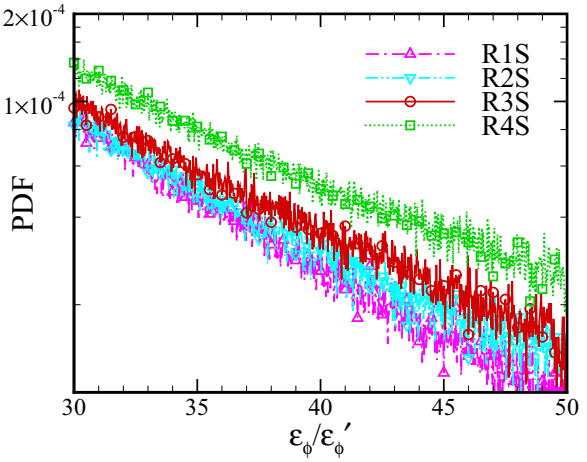

FIG. 13. The one-point PDF of the normalized scalar dissipation rate.

Figure 13 shows the probability distribution function (PDF) of the normalized scalar dissipation rate, where $\epsilon'_\phi = \sqrt{\langle(\epsilon_\phi - \langle\epsilon_\phi\rangle)^2\rangle}$ is the r.m.s. magnitude of ϵ_ϕ. It is found that the increase in the Mach number enhances the scalar dissipation occurring at large amplitudes, especially for the compressible flows.

A commonly used method for quantifying the intermittency of scalar in the dissipative range is the so-called intermittency parameter, μ_ϕ, through the autocorrelation of the scalar dissipation rate, namely,

$$\langle\epsilon_\phi(\mathbf{x})\epsilon_\phi(\mathbf{x}+\mathbf{r})\rangle \sim r^{-\mu_\phi}. \tag{3.19}$$

Figure 14 presents a log-log plot of the autocorrelations of the scalar dissipation rate, as functions of the normalized separation distance r/η, where the logarithmic bases for both horizontal and vertical axes are 10. In the rough range of $2 \leqslant r/\eta \leqslant 8$, the values of μ_ϕ are 0.63, 0.71, 0.73, and 0.76 from R1S through R4S, respectively. This means that, in the dissipative range, the intermittency of scalar becomes stronger as the Mach number increases.

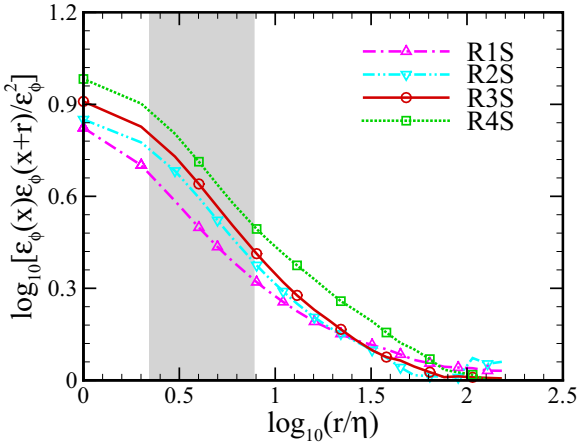

FIG. 14. Autocorrelation of scalar dissipation rate, as a function of r/η.

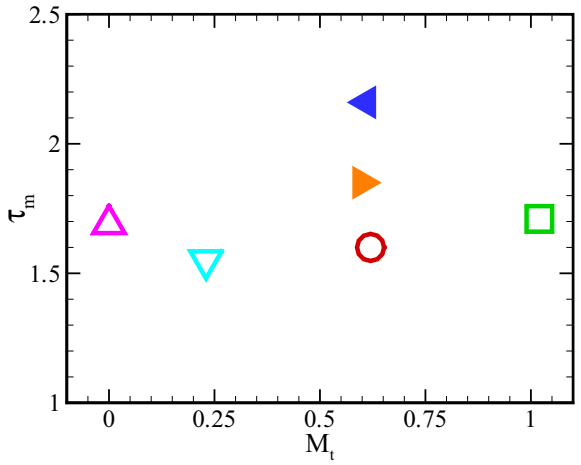

FIG. 15. Mixing time scale of scalar as a function of the turbulent Mach number. R1S: delta, R2S: gradient, R3S: circle, R4S: square, R3Ca: right-pointing triangle, and R3Cb: left-pointing triangle.

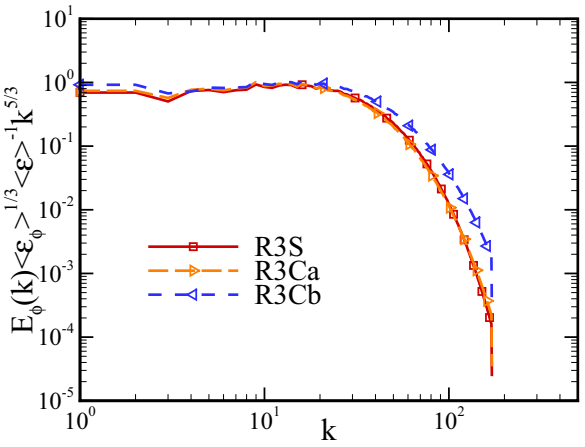

FIG. 16. Compensated spectrum of scalar according to the Obukhov-Corrsin variables, from cases of R3S, R3Ca, and R3Cb.

At the end of this subsection, we explore the dependency of the mixing time scale, τ_m, on the compressibility in Fig. 15, where τ_m is defined as

$$\tau_m \equiv \frac{E_\phi}{\langle \epsilon_\phi \rangle}. \tag{3.20}$$

It shows that, for the flows driven by the solenoidal mode of forcing, the change in the Mach number makes the mixing time scale vary slightly. In contrast, for the $M_t \approx 0.6$ compressible flows, the increase in the compressive mode of forcing leads the mixing time scale to increase significantly. This indicates that, compared with the solenoidal mode, the compressive mode is less efficient in enhancing scalar mixing.

IV. EFFECTS OF COMPRESSIBILITY: DIFFERENCE IN THE FORCING SCHEME

In this section, we discuss the effects of compressibility on compressible turbulent mixing caused by the difference in the forcing scheme. We first apply the Helmholtz decomposition [12] to the velocity field

$$u_i = u_{i,s} + u_{i,c}, \tag{4.1}$$

where $u_{i,s}$ is the solenoidal component satisfying $\partial u_{i,s}/\partial x_i = 0$, $u_{i,c}$ is the compressive component satisfying $\varepsilon_{ijk}\partial u_{k,c}/\partial x_j = 0$, and ε_{ijk} is the Levi-Civita symbol. Table III shows that the r.m.s. magnitudes of the solenoidal (u_s') and compressive (u_c') components of velocity, respectively, decreases and increases when the compressive mode of forcing increases. Therefore, the ratio of u_c' to u_s', grows significantly over the compressive mode of forcing. Furthermore, the kinetic energy dissipation rate can be divided into three parts [31]: the solenoidal dissipation rate $\epsilon_s = (\mu/\mathrm{Re})\omega_i\omega_i$, the dilatation dissipation rate $\epsilon_c = (4/3)(\mu/\mathrm{Re})\theta^2$, and the mixed dissipation rate $\epsilon_m = (2\mu/\mathrm{Re})[(\partial u_i/\partial x_j)(\partial u_j/\partial x_i) - \theta^2]$, which represents the contribution to the dissipation rate from the nonhomogeneous component of compressible flow. Here ω_i is the vorticity. It shows that when the compressive mode of forcing increases, the ensemble averages of the solenoidal and dilatation parts decreases and increases, respectively. The ensemble average of the mixed part is zero in R3S and becomes negative in R3Ca and R3Cb.

TABLE III. Helmholtz decomposition in cases R3S, R3Ca, and R3Cb.

Case	ρ'	u'	u_s'	u_c'	u_c'/u_s'	$\langle\epsilon\rangle$	$\langle\epsilon_s\rangle$	$\langle\epsilon_c\rangle$	$\langle\epsilon_m\rangle$
R3S	0.12	2.32	2.30	0.30	0.13	0.75	0.73	0.02	0.00
R3Ca	0.30	2.22	1.95	1.06	0.54	0.69	0.53	0.17	−0.01
R3Cb	0.44	2.17	1.25	1.77	1.42	0.71	0.38	0.36	−0.03

In Fig. 16 we plot the compensated scalar spectra according to the OC variables from R3S, R3Ca, and R3Cb. Similar to those shown in Fig. 2, the plateaus appear in the inertial range of $5 \leqslant k \leqslant 20$, and the values of C_{OC} are about 0.83. Throughout the entire wave number range, the scalar spectra from R3S and R3Ca overlap. In contrast, the scalar spectrum from R3Cb is higher at large scales and decays more slowly at small scales. It again proves that the compressive mode of forcing reduces the mixing of scalar in the dissipative range.

The second-order structure function of scalar increment is shown in Fig. 17, which corresponds to the scalar spectrum in wave number space. The values of the scaling constant computed from the plateaus appearing in the inertial range of $30 \leqslant r/\eta \leqslant 150$ are 0.17, 0.18, and 0.21 from R3S through R3Cb, respectively. This reveals that the growth of the compressive mode of forcing increases the scalar content, which is in agreement with the conclusion derived from the study of scalar spectrum.

Given there are density fluctuations in compressible turbulent mixing, we introduce the density weighted scalar $\Phi = \sqrt{\rho}\phi$. Then the governing equation of scalar variance is obtained as [11]

$$\frac{\partial}{\partial t}\left(\frac{\Phi^2}{2}\right) = -u_j\frac{\partial}{\partial x_j}\left(\frac{\Phi^2}{2}\right) - 2\theta\left(\frac{\Phi^2}{2}\right) - \frac{\chi}{\beta}\left(\frac{\partial\phi}{\partial x_j}\right)^2 + \frac{\chi}{\beta}\frac{1}{\sqrt{\rho}}\frac{\partial^2}{\partial x_j^2}\left(\frac{\Phi^2}{2}\right). \tag{4.2}$$

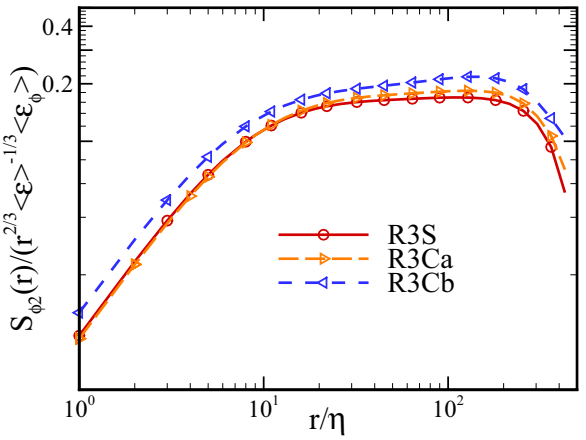

FIG. 17. Obukhov-Corrsin scaling of second-order structure function of scalar, from the cases of R3S, R3Ca, and R3Cb.

Here the terms on the right-hand-side of Eq. (4.2) are, from left to right, the advection, scalar dilatation, dissipation, and diffusion terms. In statistically homogeneous turbulence, the global average makes the diffusion term vanish. In Fig. 18 we plot the 2D contours of the scalar dilatation terms in the $z = \pi/2$ plane from R3S and R3Cb. It shows that, for R3S, the positive and negative couplings are concentrated in small-scale regions and are distributed randomly. For R3Cb, the positive coupling occupies the whole visualization domain, while the negative coupling only arises in the vicinity of the large-scale shock waves.

The 2D contours of the logarithms of the scalar dissipation rate for the same flows shown in Fig. 19 are rather different. For R3S, the outlook of the scalar dissipation field is between those for R1S and R4S visualized in Fig. 12. In contrast, for R3Cb, the motions of rarefaction and compression caused by the large-scale shock wave lead the scalar dissipation field to lack the small-scale structures. In other words, there are only the large-scale regions for low and high dissipations.

Finally, in Fig. 20 we compute the intermittency parameter by the autocorrelation of the scalar dissipation rate. In the rough range of $2.5 \leqslant r/\eta \leqslant 6.5$, the values of the intermittency parameter are $\mu_\phi = 0.73$, 0.62, and 0.59 from R3S through R3Cb, respectively. This indicates that, in the dissipative range, the intermittency of scalar becomes weaker when the compressive mode of forcing increases, which is opposite to the change of the intermittency parameter caused by the growth of the Mach number.

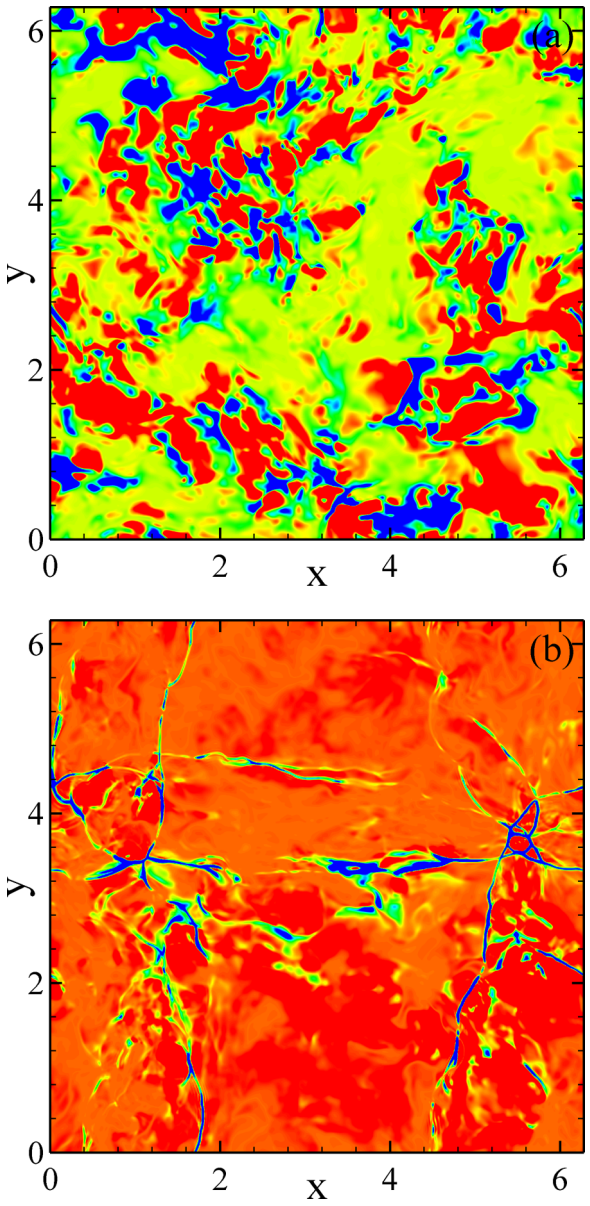

FIG. 18. Two-dimensional contours of scalar-dilatation coupling term of the scalar variance equation from (a) R3S and (b) R3Cb, in $z = \pi/2$.

V. SUMMARY AND CONCLUSIONS

In this paper, we described our systematic investigation of the effects of compressibility on passive scalar transport in compressible turbulence. The simulations were solved numerically by adopting a hybrid method of a seventh-order WENO scheme for shock regions and an eighth-order CCFD scheme for smooth regions outside shocks. Large-scale, random forcing was added to the velocity field for achieving and maintaining a statistically stationary state. The simulated flows were divided into two groups. One group was used to study the effects of compressibility because of the change in the Mach number, where the turbulent Mach number was varied from zero to unity, and the flows were driven by the solenoidal mode of forcing. The other group was used to explore the effects of compressibility due to the difference in the forcing scheme, where the turbulent Mach number was fixed at around 0.6, and the ratio of the compressive to solenoidal modes of forcing was varied from zero to 20. Our results show that, the scalar variance decreases when the Mach number increases, and the ensemble average of the scalar dissipation rate decreases when the compressive mode of forcing increases. In contrast, the r.m.s. magnitude of density fluctuations always increases as the degree of compressibility grows.

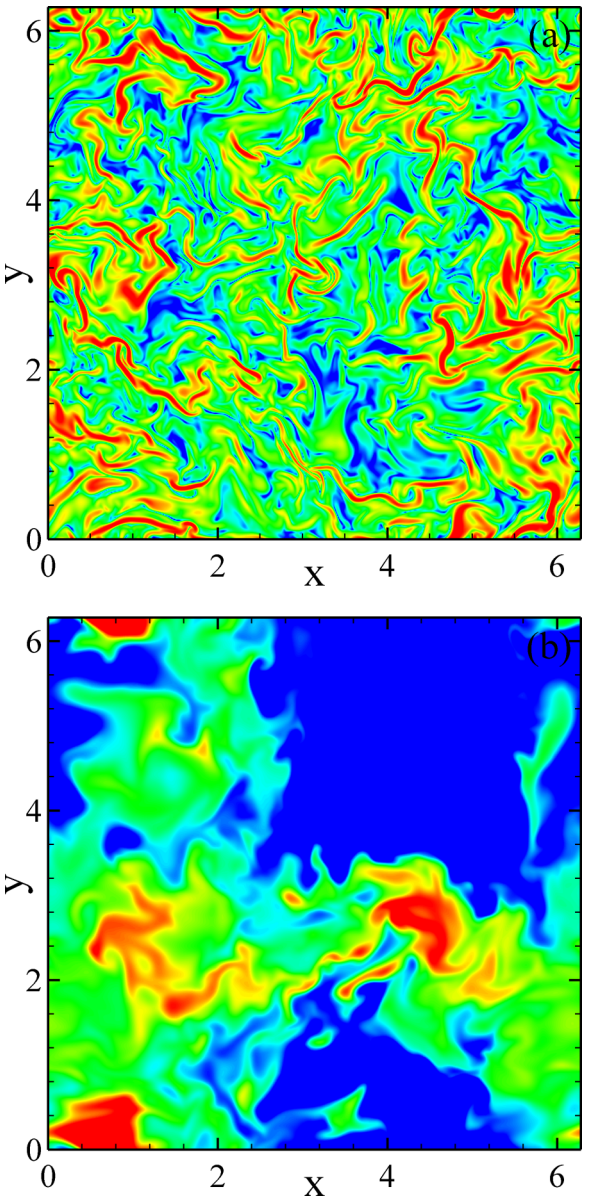

FIG. 19. Two-dimensional contours of logarithm of the dissipation term of the scalar variance equation from (a) R3S and (b) R3Cb, in $z = \pi/2$, where the logarithmic base is 10.

In the inertial range, the scalar spectrum follows the $k^{-5/3}$ power law. The effect of compressibility brings negligible contributions to the scalar spectrum and the second-order structure function of scalar increment, except for the transition zone between incompressible and compressible flows. For the mixed third-order structure function of velocity-scalar increments, our results show that the transfer of scalar flux is reduced by the transition from incompressible to compressible flows, but is enhanced by the increase in the Mach number in compressible flows. At large order numbers, the scaling exponents for the scalar and mixed velocity-scalar structure functions from the incompressible flow collapse between those from the $M_t = 1.02$ compressible flow and the $M_t = 0.9$ isothermal compressible flow [9].

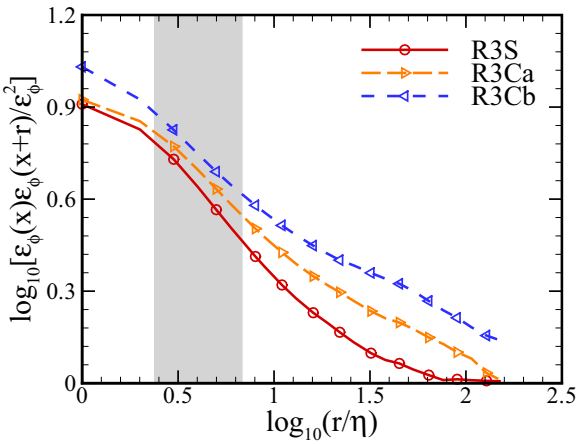

FIG. 20. Autocorrelation of scalar dissipation rate, as a function of r/η, from the cases of R3S, R3Ca, and R3Cb.

As the degree of compressibility grows, in magnitude, the skewness and flatness of scalar derivative increase, while the mixed skewness and flatness of velocity-scalar derivatives decrease. Moreover, a comparison on flatness shows that, at low degree of compressibility, the intermittency of scalar is stronger than that of velocity. However, a reversal occurs as the degree of compressibility continuously grows. The intermittency parameter, which is used to measure the intermittency of scalar in the dissipative range, increases by the growth of the Mach number and decreases by the growth of the compressive mode of forcing. The dependency of the mixing time scale on the compressibility shows that, for the driven forcing, the compressive mode is less efficient than the solenoidal mode in enhancing scalar mixing.

Finally, the 2D contour shows that, in the flow driven by the solenoidal mode of forcing, the scalar dissipation field is filled with the small-scale, highly convoluted structures, which are randomly distributed. However, in the flow driven by the compressive mode of forcing, the scalar dissipation field lacks the small-scale structures. Instead, the large-scale regions for low and high dissipations are dominated by the large-scale motions of rarefaction and compression.

In summary, the above findings reveal that the effects of compressibility, including the change in the Mach number and the difference in the forcing scheme, have pronounced influence on the small-scale statistics and field structure of passive scalar in compressible turbulence. Here, we stress that the contributions from the Mach number and the forcing scheme may be quite different. A deeper investigation on the compressible turbulent mixing with higher Mach, Reynolds, and Schmidt numbers will be carried out in the near future.

ACKNOWLEDGMENTS

This work was supported by the European Research Council Grant 339032 and the China Postdoctoral Science Foundation Grant 2015T80017. Simulations were done on the TH-1A supercomputer in Tianjin, National Supercomputer Center of China.

[1] D. M. Meyer, M. Jura, and J. A. Cardelli, Astrophys. J. **493**, 222 (1998).
[2] S. I. B. Cartledge, J. T. Lauroesch, D. M. Meyer, and U. J. Sofia, Astrophys. J. **641**, 327 (2006).
[3] R. Lu and R. P. Turco, J. Atmos. Sci. **51**, 2285 (1994).
[4] R. Lu and R. P. Turco, Atmos. Environ. **29**, 1499 (1995).
[5] S. B. Pope, Symposium on Combustion **23**, 591 (1991).
[6] Z. Warhaft, Annu. Rev. Fluid Mech. **32**, 203 (2000).
[7] M. A. de Avillez and M.-M. Mac Low, Astrophys. J. **581**, 1047 (2002).
[8] L. Pan and E. Scannapieco, Astrophys. J. **721**, 1765 (2010).
[9] L. Pan and E. Scannapieco, Phys. Rev. E **83**, 045302(R) (2011).
[10] Z.-S. She and E. Leveque, Phys. Rev. Lett. **72**, 336 (1994).
[11] Q. Ni, Phys. Rev. E **91**, 053020 (2015).
[12] Q. Ni, Y. Shi, and S. Chen, arXiv:1505.02685.
[13] Q. Ni and S. Chen, Phys. Rev. E **86**, 066307 (2012).
[14] Q. Ni and S. Chen, arXiv:1506.04179.
[15] J. Wang, L.-P. Wang, Z. Xiao, Y. Shi, and S. Chen, J. Comput. Phys. **229**, 5257 (2010).
[16] Q. Ni, Y. Shi, and S. Chen, Phys. Fluids **25**, 075106 (2013).
[17] W. Sutherland, Philos. Mag. Suppl. **5**, 507 (1992).
[18] D. S. Balsara and C. W. Shu, J. Comput. Phys. **160**, 405 (2000).
[19] S. K. Lele, J. Comput. Phys. **103**, 16 (1992).
[20] K. Gawedzki and M. Vergassola, Physica D **138**, 63 (2000).
[21] A. N. Kolmogorov, Dokl. Akad. Nauk SSSR **30**, 9 (1941).
[22] A. N. Kolmogorov, Dokl. Akad. Nauk SSSR **32**, 16 (1941).
[23] L.-P. Wang, S. Chen, J. G. Brasseur, and J. C. Wyngaard, J. Fluid Mech. **309**, 113 (1996).
[24] A. M. Obukhov, Izv. Geogr. Geophys. **13**, 281 (1949).
[25] S. Corrsin, J. Appl. Phys. **22**, 469 (1951).
[26] L. Mydlarski and Z. Warhaft, J. Fluid Mech. **358**, 135 (1998).
[27] L.-P. Wang, S. Chen, and J. C. Wyngaard, J. Fluid Mech. **400**, 163 (1999).
[28] A. M. Yaglom, Dokl. Akad. Nauk SSSR **69**, 6 (1949).
[29] R. Benzi, S. Ciliberto, R. Tripiccione, C. Baudet, F. Massaioli, and S. Succi, Phys. Rev. E **48**, R29 (1993).
[30] T. Watanabe and T. Gotoh, New J. Phys. **6**, 40 (2004).
[31] Y. Andreopoulos, J. H. Agui, and G. Briassulis, Annu. Rev. Fluid Mech. **32**, 309 (2000).